

# Epitaxial Strain Control of Relaxor Ferroelectric Phase Evolution

Jieun Kim, Hiroyuki Takenaka, Yubo Qi, Anoop R. Damodaran, Abel Fernandez, Ran Gao, Margaret R. McCarter, Sahar Saremi, Linh Chung, Andrew M. Rappe, and Lane W. Martin\*

Understanding and ultimately controlling the large electromechanical effects in relaxor ferroelectrics requires intimate knowledge of how the local-polar order evolves under applied stimuli. Here, the biaxial-strain-induced evolution of and correlations between polar structures and properties in epitaxial films of the prototypical relaxor ferroelectric  $0.68\text{PbMg}_{1/3}\text{Nb}_{2/3}\text{O}_3-0.32\text{PbTiO}_3$  are investigated. X-ray diffuse-scattering studies reveal an evolution from a butterfly- to disc-shaped pattern and an increase in the correlation-length from  $\approx 8$  to  $\approx 25$  nm with increasing compressive strain. Molecular-dynamics simulations reveal the origin of the changes in the diffuse-scattering patterns and that strain induces polarization rotation and the merging of the polar order. As the magnitude of the strain is increased, relaxor behavior is gradually suppressed but is not fully quenched. Analysis of the dynamic evolution of dipole alignment in the simulations reveals that, while, for most unit-cell chemistries and configurations, strain drives a tendency toward more ferroelectric-like order, there are certain unit cells that become more disordered under strain, resulting in stronger competition between ordered and disordered regions and enhanced overall susceptibilities. Ultimately, this implies that deterministic creation of specific local chemical configurations could be an effective way to enhance relaxor performance.

Relaxor ferroelectrics have attracted considerable attention due to their intriguing dielectric and piezoelectric properties.<sup>[1,2]</sup> Broad dielectric response with temperature and strong dielectric relaxation with frequency have long been attributed to the formation of polar nanoregions (PNRs) in a nonpolar matrix<sup>[1]</sup> where the Burns temperature ( $T_b$ )<sup>[3]</sup> and dielectric maximum temperature ( $T_m$ ) are thought to be related to the formation and onset of the slowing-down of the dynamics of the PNRs.<sup>[1,3]</sup>

Alternatively, molecular-dynamics (MD) simulations have shown that relaxors can be interpreted as exhibiting a multi-domain state without a nonpolar matrix (i.e., polar nanodomains or PNDs).<sup>[4]</sup> The exact nature of order in relaxors, however, remains an ongoing debate<sup>[5]</sup> and, in turn, new approaches to study these complex materials are required to further illuminate the structure and how it can be controlled and can impact material properties.<sup>[5–9]</sup>

In any case, it is essential to understand the evolution of the polar structure in relaxors (be they PNRs or PNDs) under applied stimuli as these are key to understanding relaxor behavior and large electromechanical effects in relaxors. Over the years, X-ray and neutron diffuse-scattering measurements have emerged as an essential tool to study the structural signatures of relaxor behavior<sup>[10–19]</sup> and studies on single-crystal relaxors have investigated the evolution of polar regions/domains (e.g., size, morphology) and suggested that they alter their size<sup>[14–17]</sup> and orientation<sup>[18]</sup> under different external stimuli. For example, under applied electric fields, which were expected to enhance polar order, the local order was found to align perpendicular to the field<sup>[18]</sup> and induce an asymmetry in the lattice dynamics<sup>[19]</sup> that could ultimately be responsible for the large electromechanical effects.<sup>[20]</sup> Other studies used pressure to push the material in the opposite direction—to destabilize polar order<sup>[17]</sup>—and even induce a crossover from

J. Kim, Dr. A. R. Damodaran, A. Fernandez, R. Gao, S. Saremi, L. Chung, Prof. L. W. Martin  
Department of Materials Science and Engineering  
University of California  
Berkeley, Berkeley, CA 94720, USA  
E-mail: lwmartin@berkeley.edu

Dr. H. Takenaka  
Department of Physics  
University of Nebraska  
Lincoln, Lincoln, NE 68588, USA

 The ORCID identification number(s) for the author(s) of this article can be found under <https://doi.org/10.1002/adma.201901060>.

Dr. Y. Qi, Prof. A. M. Rappe  
Department of Chemistry  
University of Pennsylvania  
Philadelphia, PA 19104-6323, USA

M. R. McCarter  
Department of Physics  
University of California  
Berkeley, Berkeley, CA 94720, USA

Prof. L. W. Martin  
Materials Sciences Division  
Lawrence Berkeley National Laboratory  
Berkeley, CA 94720, USA

DOI: 10.1002/adma.201901060

ferroelectric to relaxor behavior.<sup>[21]</sup> While such studies illustrate what happens when polar order is destabilized without additional compositional fluctuations,<sup>[17,21]</sup> analogous experiments where one enhances polar order with pressure (e.g., via uniaxial compression<sup>[22,23]</sup> or negative pressure<sup>[24]</sup>) have progressed slowly. Such studies, however, have the potential to address a number of important questions, including whether enhancing ferroelectric order without changing the composition can ultimately drive relaxors to become normal ferroelectrics.<sup>[18]</sup>

In this spirit, biaxial-compressive strain in epitaxial thin films provides a pathway to achieve such desired stabilization of polar order. While the use of epitaxial constraints to manipulate ferroelectric order has been widely demonstrated,<sup>[25–27]</sup> little of that work has focused on relaxors.<sup>[28–32]</sup> Theoretical studies have proposed that strain can significantly alter the morphologies of local-polar order and the direction of dipoles within them.<sup>[28]</sup> But experimental studies have provided contradicting observations of the effect of epitaxial strain<sup>[29–32]</sup>; some suggest that compressive strain increases  $T_m$ <sup>[29,30]</sup> and induces ferroelectricity<sup>[31]</sup> while others claim that compressive strain decreases  $T_m$  and favors the relaxor state.<sup>[32]</sup> These discrepancies likely arise from the use of partially relaxed (i.e., inhomogeneously strained) films<sup>[33]</sup> and from insufficient study of essential relaxor characteristics (e.g., local correlations and dynamics, diffuse-scattering, frequency dispersion of  $T_m$ , etc.).<sup>[4,8,34,35]</sup> The work herein directly addresses these issues.

Here, we develop a comprehensive picture of the relationship between epitaxial strain, local polar structure, and properties in films of the prototypical relaxor  $0.68\text{PbMg}_{1/3}\text{Nb}_{2/3}\text{O}_3\text{--}0.32\text{PbTiO}_3$  (PMN-PT) using a combination of synchrotron-based X-ray diffuse-scattering, dielectric and ferroelectric properties, and MD simulations. Coherently strained PMN-PT films were produced under three different compressive-strain conditions (−0.5%, −1.0%, and −1.5%). X-ray diffuse-scattering studies reveal a classic butterfly-shaped pattern only in the lowest strain state (−0.5%) which evolves into a disc-shaped pattern under intermediate (−1.0%) and high (−1.5%) strains. This change is accompanied by an increase in the correlation length from  $\approx 8$  to  $\approx 25$  nm. MD simulations reveal the origin of the changes in the diffuse-scattering patterns and that strain induces polarization rotation and the merging of domains. This corresponds to a change in the morphology of the domain structure from small, complex multidomains with low-angle domain walls to larger, up- and down-poled domains with disordered high-angle domain walls. The changes in the domain structure are accompanied by changes in the macroscopic properties. Dielectric measurements reveal that as the compressive strain increases,  $T_b$ ,  $T_m$ , and the intermediate temperature  $T^*$  increase while the frequency dispersion of  $T_m$  decreases, suggesting that increased strain weakens, but does not fully quench, relaxor behavior. Consistent with this, polarization-electric field hysteresis loops reveal an increase in the saturation polarization and the coercive field in the intermediate-strain state, but, surprisingly, this does not occur at the expense of the electromechanical response which is shown to be enhanced. Analysis of the dynamic evolution of dipole alignment in the simulations reveals that while, for most unit-cell chemistries and configurations strain drives a tendency toward more ferroelectric-like order, there are certain unit cells which

become more disordered under strain, resulting in stronger competition between ordered and disordered regions and enhanced overall susceptibility to applied stimuli. Ultimately, this implies that deterministic creation of specific local chemical configurations could be an effective way to enhance relaxor performance even in known materials.

55 nm PMN-PT/25 nm  $\text{Ba}_{0.5}\text{Sr}_{0.5}\text{RuO}_3/\text{NdScO}_3$ ,  $\text{SmScO}_3$ , and  $\text{GdScO}_3$  (110) (corresponding to in-plane, biaxial-compressive strains of −0.5%, −1.0%, and −1.5% and termed “low”, “intermediate”, and “high” strain in this study, respectively) heterostructures were synthesized via pulsed-laser deposition (Experimental Section). X-ray diffraction studies (Experimental Section) reveal that the films are high-quality, single-phase, and epitaxial (Figure 1a). A zoom-in about the PMN-PT 002-diffraction condition reveals that the out-of-plane lattice parameter of the PMN-PT films systematically increases with increasing in-plane compressive strain (Figure 1b). Analysis of the full-width-at-half-maximum (FWHM) of rocking curves about the PMN-PT 002-diffraction condition (Experimental Section; Figure S1, Supporting Information) reveals values almost an order of magnitude smaller than those in the literature,<sup>[29,30,36]</sup> attesting to the quality of the heterostructures. Reciprocal space mapping (RSM) studies (Experimental Section; Figure S2, Supporting Information) reveal that all films are coherently strained to the substrates. To extract information about the structure of the local-polar order, diffuse-scattering data was obtained from three-dimensional, synchrotron-based RSM studies (Experimental Section). For brevity, we focus on the analysis of diffuse-scattering about the PMN-PT 002-diffraction condition (Figure 1c–e), but data for other diffraction peaks are also provided (Experimental Section; Figure S3, Supporting Information). Temperature-dependent studies were also completed to assure that the diffuse-scattering intensity arises from the polar structures, and it was confirmed that this intensity disappears in the paraelectric phase (Experimental Section; Figures S4 and S5, Supporting Information). To visualize the effect of strain on the diffuse-scattering, the data are represented as iso-intensity contours using cutoff intensities that effectively represent the diffuse-scattering shape for different strain states, and variations are clearly visible. For comparison with the literature, where the diffuse-scattering is usually reported in two-dimensional representations,<sup>[10–19]</sup> data for the  $0kl$  plane which cuts through the primary Bragg reflections (shaded plane, Figure 1c–e) are also provided (Figure 1f–h). Low-strain heterostructures exhibit a classic butterfly-shaped diffuse-scattering pattern about the PMN-PT 002-diffraction condition, with diffuse rods extending along the  $[011]$  and  $[0\bar{1}1]$  (Figure 1c,f). Measurement of diffuse-scattering about the PMN-PT 022-diffraction condition reveals the absence of a diffuse rod along the  $[011]$  (Experimental Section; Figure S3a, Supporting Information), confirming important features of the diffuse-scattering of single-crystal relaxors<sup>[13]</sup> and that such films can serve as a reference for further discussions of strain-induced effects. Inspection of intermediate-strain heterostructures (Figure 1d,g) reveals that the butterfly-shaped diffuse-scattering has evolved into a disc-shaped pattern. In high-strain heterostructures, the diffuse-scattering (Figure 1e,h) exhibits a similar disc-shaped pattern, but the  $k$ -space extent of the pattern is much smaller, and the overall shape is more isotropic, indicating reduced disorder.

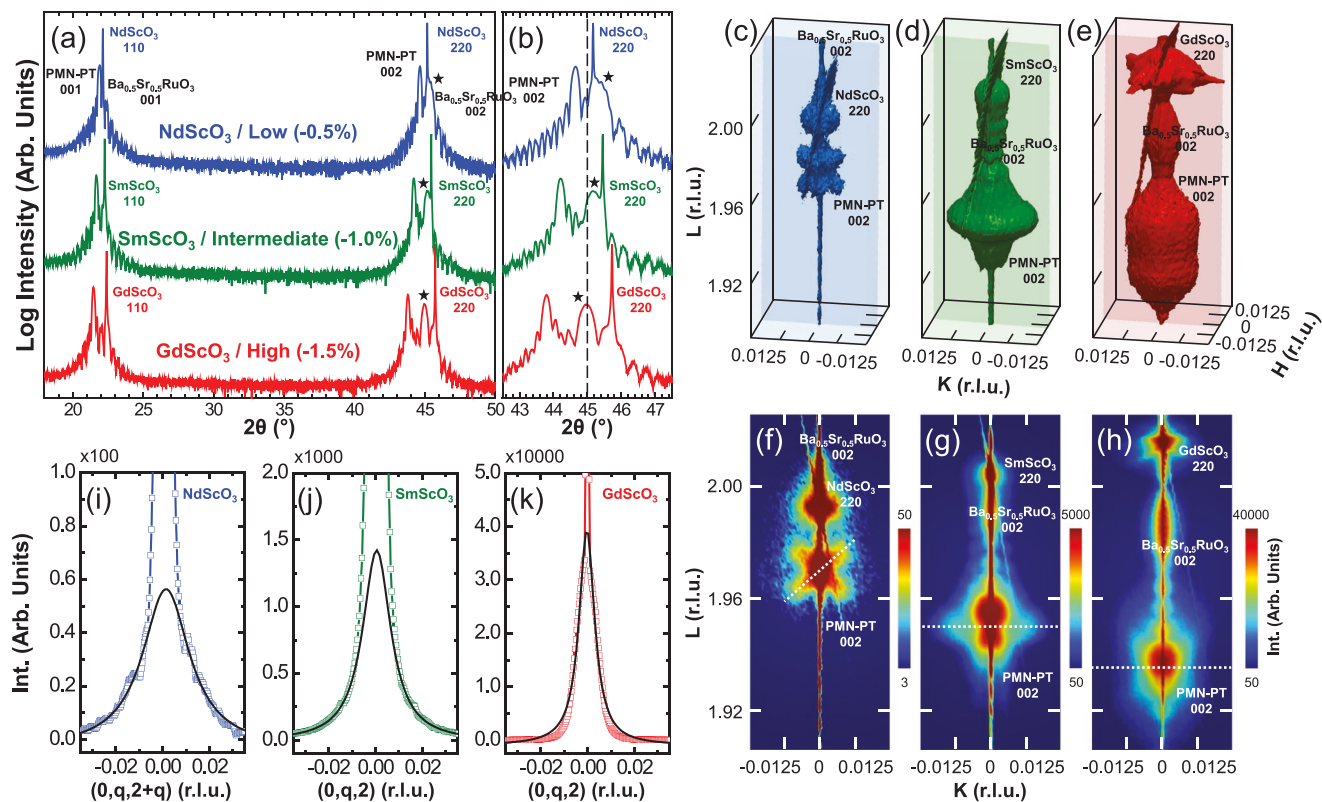


**Figure 1.** Characterization of crystal structure and diffuse-scattering. a) Wide-angle  $\theta$ - $2\theta$  X-ray diffraction line scans of epitaxial  $0.68\text{Pb}(\text{Mg}_{1/3}\text{Nb}_{2/3})\text{O}_3$ - $0.32\text{PbTiO}_3$  (PMN-PT) thin films on various substrates. b) A zoom-in about the PMN-PT 002-diffraction condition. The  $\star$  denotes peaks for the  $\text{Ba}_{0.5}\text{Sr}_{0.5}\text{RuO}_3$  002-diffraction condition and the dashed line denotes the position of the peak for bulk PMN-PT. c–e) 3D reciprocal space mapping studies about the PMN-PT 002-diffraction condition for heterostructures grown on: c)  $\text{NdScO}_3$ , d)  $\text{SmScO}_3$ , and e)  $\text{GdScO}_3$  (110) substrates. f–h) 2D KL-cuts corresponding to shaded planes in (c)–(e) for heterostructures grown on: f)  $\text{NdScO}_3$ , g)  $\text{SmScO}_3$ , and h)  $\text{GdScO}_3$  (110) substrates. i–k) Diffuse-scattering intensity profiles extracted along the dashed lines in (f)–(h) for heterostructures grown on: i)  $\text{NdScO}_3$ , j)  $\text{SmScO}_3$ , and k)  $\text{GdScO}_3$  (110) substrates. The open squares show the experimental data and the solid lines are fits to the Lorentzian profile. Note that the directions of the diffuse intensities are different between (f) (along [011]) and (g,h) (along [010]) due to the changes in the diffuse-scattering pattern.

To examine the strain-induced changes in the correlation-length ( $\xi$ ), which is a measure of the average size of the local-polar order, diffuse-scattering intensity line profiles (along the [011] for the low- and along the [010] for the intermediate- and high-strain heterostructures) were fitted with a Lorentzian function<sup>[14]</sup> (solid lines, Figure 1i–k)

$$I_{\text{diff}} = \frac{I_0 \Gamma}{\pi (q^2 + \Gamma^2)} \quad (1)$$

where  $I_0$  is the integrated diffuse-scattering intensity,  $\Gamma$  is the half-width-at-half-maximum (HWHM) of the Lorentzian profile and the inverse of  $\xi$ , and  $q$  is the length of the wave vector measured from the Bragg positions. The fitting parameters  $I_0$  and  $\Gamma$  (and  $\xi = 1/\Gamma$ ) for all heterostructures are summarized (Table 1).  $\xi$  for the low-strain heterostructures was found to be  $\approx 8$  nm, in good agreement with previous studies.<sup>[4,15,16]</sup> It is noted that  $\xi$  systematically increases as the magnitude of the strain increases, accompanied by similar trends in  $I_0$ . The increase in  $\xi$  is due to stronger dipole alignment with increasing strain.<sup>[37,38]</sup> Furthermore, recalling that such butterfly-shaped diffuse-scattering can arise from multidomain structures with small domain sizes

( $\approx 6$  nm) and a high density of low-angle domain walls ( $\approx 60^\circ$ ) (without a nonpolar matrix),<sup>[4]</sup> it can be hypothesized that the increase in  $\xi$  with strain arises from a narrowing of the distribution (size, shape) and merging of small-sized domains into larger domains. That the heterostructures still exhibit diffuse-scattering under large strains (albeit of a different shape) suggests that relaxors do not simply transform into a ferroelectric phase under large compressive strains.

In order to confirm this hypothesis and gain physical insight into the strain-induced changes observed in the experiments,

**Table 1.** Summary of fitting parameters for diffuse scattering for PMN-PT under compressive strains from  $-0.5\%$  to  $-1.5\%$ .

Substrate	Integ. Int. ( $I_0$ )	HWHM $\Gamma$ [ $\text{\AA}^{-1}$ ]	Corr. Length $\xi$ [ $\text{\AA}$ ]	Diff. Scatt. Shape
$\text{NdScO}_3$ ( $-0.5\%$ )	2.3	0.01229	81.4	Butterfly
$\text{SmScO}_3$ ( $-1.0\%$ )	32.2	0.00748	133.7	Disc
$\text{GdScO}_3$ ( $-1.5\%$ )	508.2	0.00403	248.1	Disc

we perform MD simulations (Experimental Section) as a function of biaxial-compressive strain to probe the evolution of the domain structures, extract the corresponding diffuse-scattering patterns, and study the spatial correlation between polar units. Here,  $x$ ,  $y$ , and  $z$  will be used to denote the in-plane [100] and [010] and out-of-plane [001], respectively. First, we visualize the evolution of the polar structures using snapshots from large-scale  $72 \times 72 \times 72$  unit-cell ( $1.866 \times 10^6$  atoms) MD simulations (Figure 2a–c) which show that there is a significant change in the domain structure with strain (here we show the  $P_x$ ,  $P_y$ , and  $P_z$  polarization components). In the low-strain state (Figure 2a), the domain structure matches closely that expected for bulk<sup>[4]</sup> and comprises multiple small domains where the direction of polarization changes by  $\approx 60^\circ$ – $80^\circ$  across the domain boundaries. Transitioning to the intermediate- (Figure 2b) and high-strain states (Figure 2c), the domain structure changes to net up- and down-poled domains, where  $P_x$  and  $P_y$  are small in magnitude and weakly correlated compared to  $P_z$ . Consistent with the experiments, the average domain size also increases. The  $P_z$  component reveals that the domain walls are aligned nearly parallel to  $\pm z$  and have irregular shapes in the intermediate-strain

state that become less tortuous in the high-strain state. In turn, we can extract the expected diffuse-scattering patterns from these domain structures (Experimental Section, Figure 2d–f). Consistent with the experimental observations, only the low-strain state (Figure 2d) exhibits a butterfly-shaped diffuse-scattering pattern while the intermediate- (Figure 2e) and high-strain states (Figure 2f) exhibit disc-shaped patterns. Consequently, we attribute the changes in the diffuse-scattering pattern with strain to changes in the domain structure.

The MD simulations are rich with insight into how strain impacts the evolution of local-polar order. For example, one can extract the so-called time-delay-averaged-correlation angle, or the angle formed between the electric dipole of a given lead ion with that of the  $n$ th ( $n = 1$ – $30$ ) nearest-neighbor lead ion in all three directions (Experimental Section, Figure 3a–f). While the MD snapshots (Figure 2a–c) pictorially illustrate the domain patterns, the correlation-angle distributions describe the probability that a given angle is formed between dipole pairs anywhere within the supercell. Correlation-angle distributions for highly correlated (i.e., nearly parallel) configurations will be centered close to  $0^\circ$  and the center value will increase for

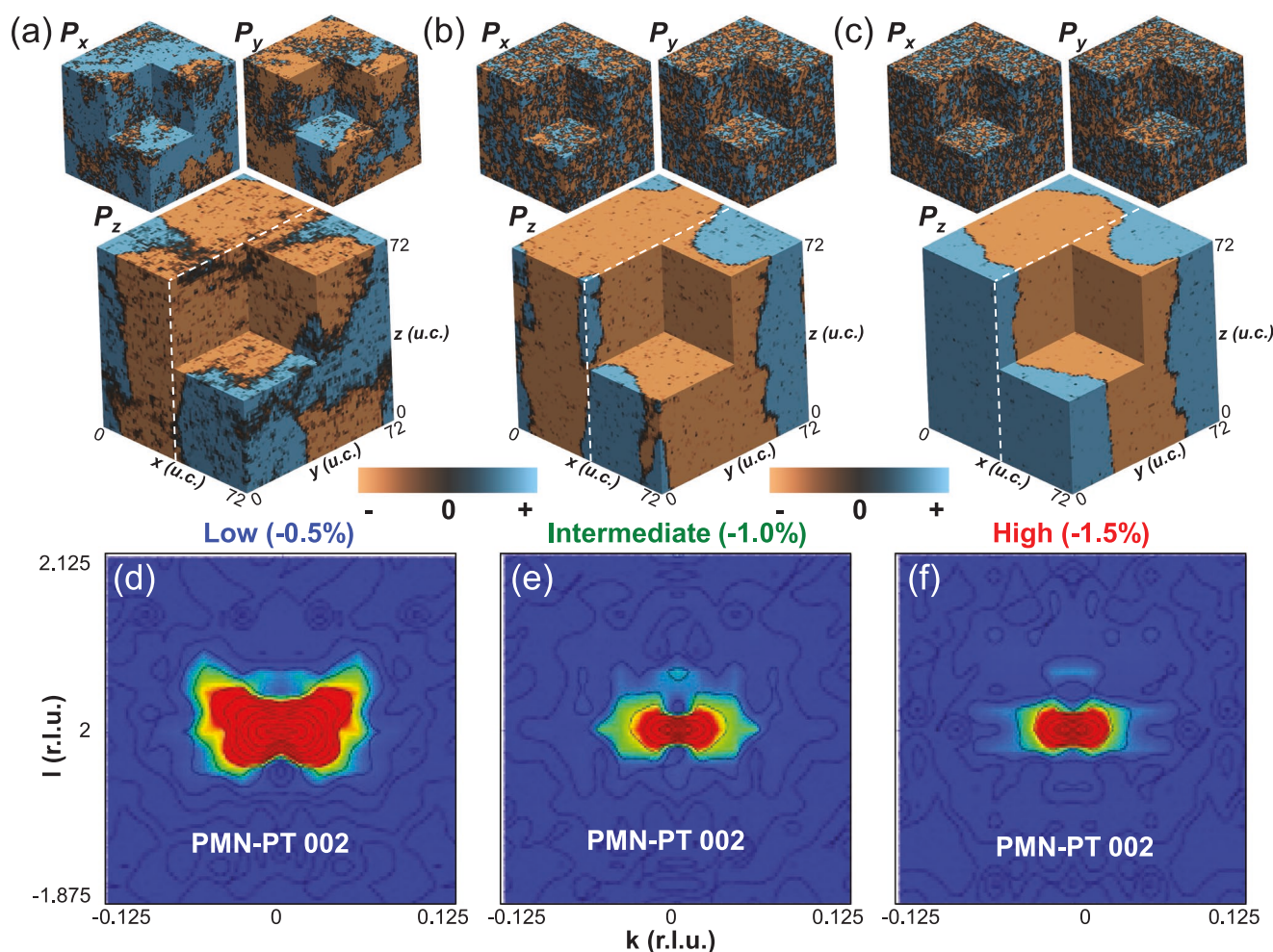


**Figure 2.** MD simulations of strain-induced domain-structure and diffuse-scattering evolution. a–c) 3D MD simulations showing  $P_x$ ,  $P_y$ , and  $P_z$  polarization components for the: a) low-, b) intermediate-, and c) high-strain states. d–f) Corresponding simulated diffuse-scattering patterns about the PMN-PT 002-diffraction condition for PMN-PT in the: d) low-, e) intermediate-, and f) high-strain states.

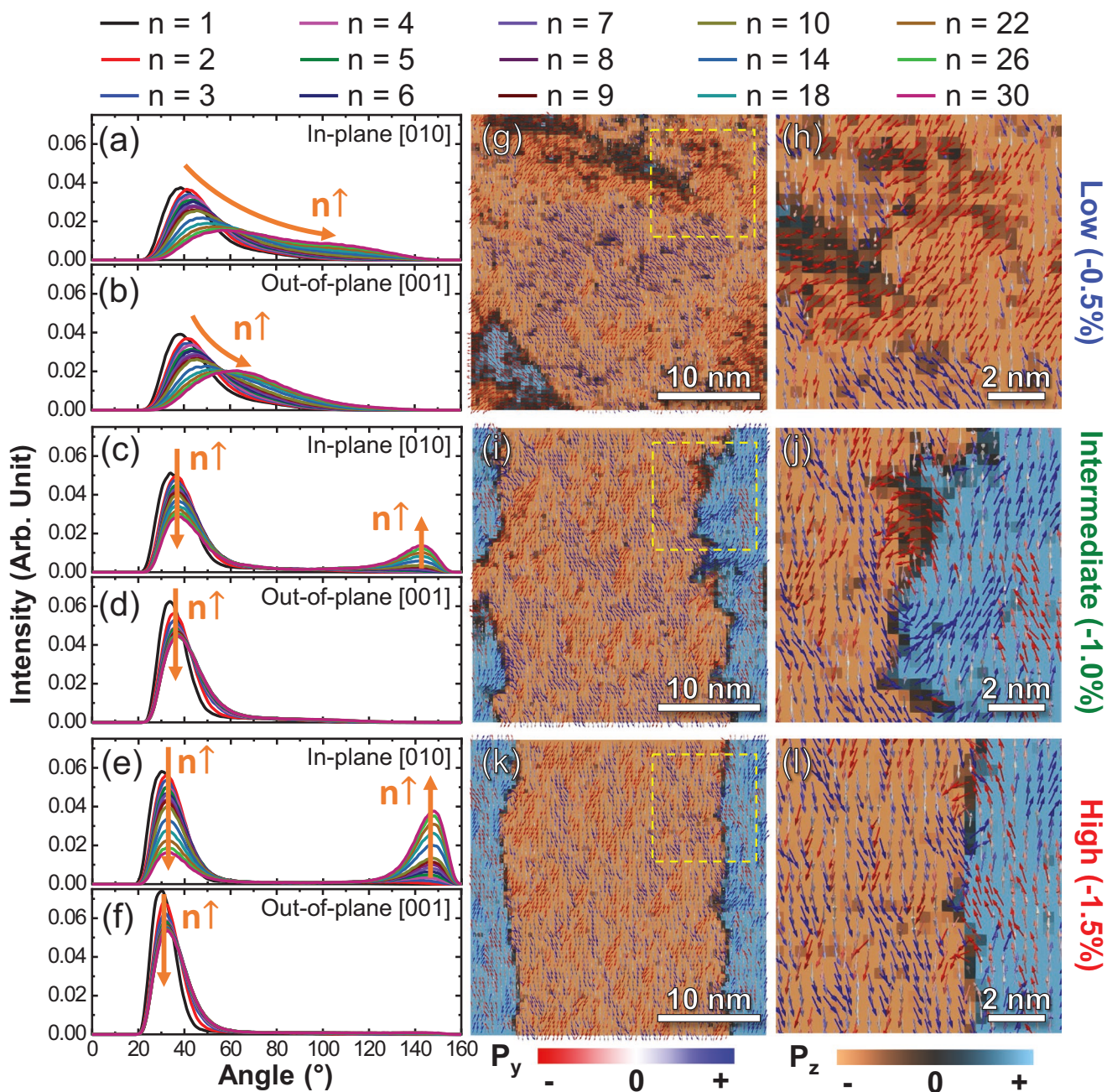


**Figure 3.** Correlation-angle distribution and domain-structure evolution with strain. a–f) Correlation-angle distribution for heterostructures in the low- (along the in-plane [010] (a) and out-of-plane [001] (b)), intermediate- (along the in-plane [010] (c) and out-of-plane [001] (d)), and high-strain states (along the in-plane [010] (e) and out-of-plane [001] (f)) up to the 30th nearest-neighbor cells. g–l) Maps of local polarization dipoles (represented as arrows for each unit cell where the color is set by the  $P_y$  component as indicated in the noted scale) in a  $yz$  cut through the center of the simulation cell where the background color scale is dictated by the  $P_z$  component for the low-strain (g,h), intermediate-strain (i,j), and high-strain (k,l) states. (h), (j), and (l) correspond to the boxed regions in (g), (i), and (k), respectively.

increasingly disordered configurations. For brevity, only the correlations along the in-plane  $y$  and out-of-plane  $z$  directions are shown herein because of the close similarity between the distributions along  $x$  and  $y$  (full data are provided in Figure S6, Supporting Information). Such distributions can be paired with real-space images of the local-polar order which can ultimately inform us about the origin of the diffuse scattering. To do this, we provide maps of the dipoles (represented as arrows for each

unit cell where the color is set by the  $P_y$  component as indicated in the noted scale) in a  $yz$  cut through the center of the simulation cell (dotted lines, Figure 2a–c) where the background color scale is set by the  $P_z$  component (Figure 3g–l).

Beginning with the low-strain state, both the in-plane (Figure 3a) and out-of-plane (Figure 3b) correlation-angle distributions shift from being centered at  $\approx 40^\circ$  for near neighbors (small values of  $n$ ) to being centered at  $\approx 70^\circ$  for distant

neighbors. This indicates two things: first, that relaxors are composed of weakly correlated dipoles and, second, that there are multiple small-sized domains separated by  $\approx 60^\circ\text{--}80^\circ$  domain boundaries (Figure 3g,h). Interestingly, the correlation-angle distributions show broader profiles along the in-plane as compared to out-of-plane directions, especially for  $n > 18$  ( $r_{\text{pb-pb}} > 7.2$  nm). This is due to the geometrical confinement imposed by strain and is consistent with the smaller vertical indentations in the butterfly-shaped diffuse-scattering pattern (Figure 2d). In the intermediate- (Figure 3c,d) and high-strain states (Figure 3e,f), however, the correlation-angle distributions are distinctly different. First, there are bimodal and unimodal distributions for the in-plane and out-of-plane directions, respectively. For the low-angle response, the peaks shift to lower angles relative to the peaks in the low-strain state for all values of  $n$  probed—confirming that strain induces stronger dipole correlations. At larger  $n$  values ( $n \geq 10$ ), the in-plane correlation-angle distributions (Figure 3c,e) evolve to exhibit two distinct peaks (with the high-angle peak being centered at  $\approx 140^\circ\text{--}150^\circ$ ). In real space (Figure 3i–l), this corresponds to the formation of domains that are elongated along the out-of-plane direction such that there is a single domain along the out-of-plane directions (hence the unimodal distribution) and various net up- and down-poled domains in the in-plane direction separated by high-angle ( $\approx 140^\circ$ ) domain boundaries (hence the bimodal distribution). This is consistent with the experimentally observed disc-shaped

diffuse-scattering patterns which arise from disorder in the in-plane directions only. Closer examination of the domain-wall regions (Figure 3j,l) reveals that the domain walls are sharpened with increasing strain, corresponding to a reduction of the intensity of the correlation-angle distributions at intermediate angles ( $70^\circ\text{--}100^\circ$ ) from the intermediate- (Figure 3c,d) to the high-strain states (Figure 3e,f). Interestingly, we also observe vortex-like dipole configurations at domain walls in both the intermediate- and high-strain states (Figure 3j,l). Such vortex formation likely arises from the competition between the intrinsic disorder of polarization expected in the relaxor and the driving force for correlation induced by the epitaxial constraints. These MD simulations provide an important look at the real-space structure of the relaxors that gives rise to the different diffuse-scattering patterns and helps contextualize how the strain drives changes in the local-polar order.

Having established the structural changes induced by the biaxial-compressive strain, we now examine how strain influences the macroscopic properties. Using symmetric metal-oxide capacitor structures (Experimental Section), the dielectric and ferroelectric response of the heterostructures was measured as a function of frequency and temperature (Experimental Section). All heterostructures were also found to exhibit well-saturated, slim polarization-electric field hysteresis loops at room-temperature; typical of relaxor ferroelectrics (Figure 4a). The coercive field, however, increases correspondingly with the

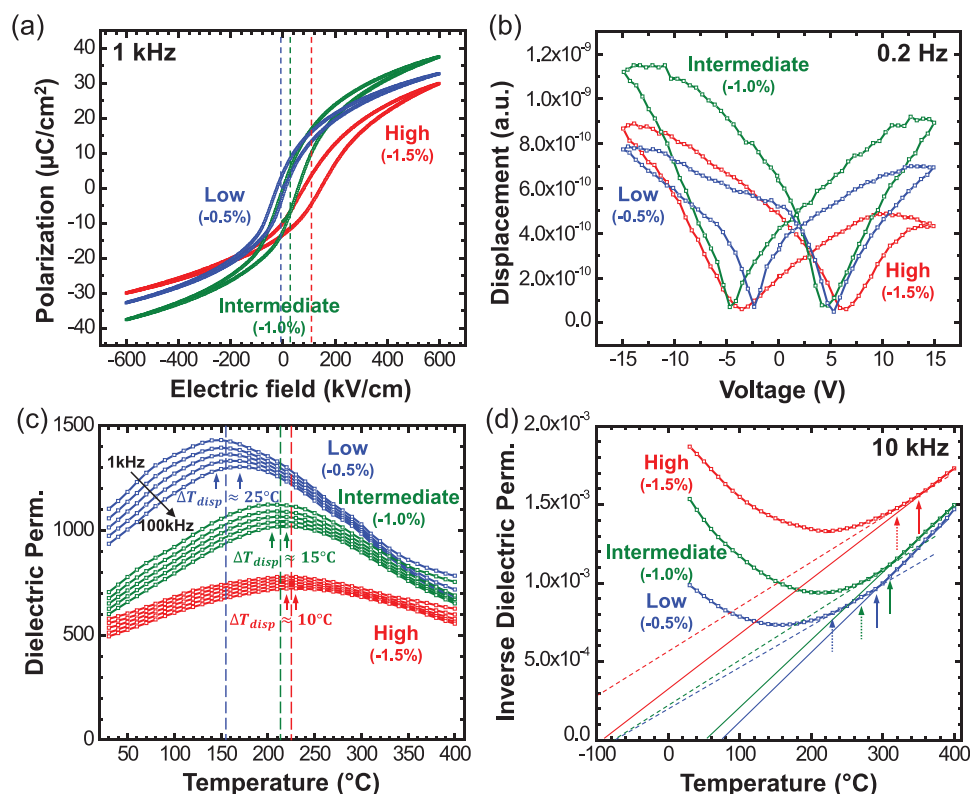


**Figure 4.** Ferroelectric, piezoelectric, and dielectric properties. a) Polarization–electric field hysteresis loops measured at a frequency of 1 kHz at room-temperature. b) Piezoelectric displacement–voltage bipolar hysteresis loops measured at a frequency of 0.2 Hz at room-temperature via piezoresponse force microscopy. c) Dielectric permittivity as a function of temperature and frequency (1–100 kHz);  $T_m$  is marked with a dashed line and  $T_m$  for 1 and 100 kHz measurement frequencies are marked by arrows on the left and right, respectively. d) Inverse-dielectric permittivity as a function of temperature, shown here at 10 kHz, where  $T_b$  and  $T^*$  are marked with solid and dashed lines, respectively.

**Table 2.** Summary of critical temperatures and fitting parameters for diffuse scattering for PMN-PT under compressive strains from  $-0.5\%$  to  $-1.5\%$ .

Substrate	$T_m^{10\text{kHz}}$ [°C]	$T^*$ [°C]	$T_b$ [°C]
NdScO <sub>3</sub> ( $-0.5\%$ )	155	230	290
SmScO <sub>3</sub> ( $-1.0\%$ )	215	270	310
GdScO <sub>3</sub> ( $-1.5\%$ )	225	320	350

change in the domain structure and is lower for the low-strain heterostructures with traditional multidomain structures and higher for the intermediate- and high-strain heterostructures with quasiperiodic up- and down-poled domains (Figure 4a). Of particular note is that both the saturation polarization and the electromechanical response (Experimental Section) are enhanced for the intermediate-strain heterostructures (Figure 4b). The temperature-dependent dielectric permittivity (Figure 4c) for the low-strain heterostructures shows typical relaxor behavior, with  $T_m^{10\text{kHz}} \approx 155$  °C; close to that of bulk PMN-PT.<sup>[39]</sup> Upon increasing the strain,  $T_m^{10\text{kHz}}$  shifts to  $\approx 210$  °C and  $\approx 225$  °C for the intermediate- and high-strain heterostructures, respectively. The frequency dispersion of  $T_m$ , which is defined as  $\Delta T_{\text{disp}} = \Delta T_m^{100\text{kHz}} - \Delta T_m^{1\text{kHz}}$  and characterizes the strength of the relaxor behavior,<sup>[35]</sup> is also found to be reduced with strain, going from  $\approx 25$  °C to  $\approx 15$  °C to  $\approx 10$  °C for the low-, intermediate-, and high-strain heterostructures, respectively, suggesting weaker relaxor (stronger ferroelectric<sup>[37,38]</sup>) character. The shift in  $T_m$  is also accompanied by reduced dielectric response. Plotting the inverse of the permittivity versus temperature reveals the evolution of  $T_b$  and  $T^*$  (Figure 4d).  $T_b$  and  $T^*$  are identified as the temperatures at which the first and second deviations from Curie–Weiss behavior appear in the temperature-dependent measurement of properties that are sensitive to the presence of local polarization<sup>[3,40]</sup> which can be either dynamic, static, or a mixture of both.<sup>[8]</sup>  $T_b$  changes from  $\approx 290$  °C to  $\approx 350$  °C while  $T^*$  changes from  $\approx 230$  °C to  $\approx 320$  °C from the low- to high-strain heterostructures. The changes in  $T_b$ ,  $T^*$ ,  $T_m$ , and  $\Delta T_{\text{disp}}$  are summarized (Table 2). To summarize, as we increase the magnitude of the compressive strain, we first drive a transformation of the domain structure of the relaxor toward a more ferroelectric-like response. This is accompanied by an expected increase in  $T_m$ , a decrease in the magnitude of the dielectric permittivity and  $\Delta T_{\text{disp}}$ , and an enhancement of the saturation polarization and coercive field. What is surprising, however, is the corresponding increase in the electromechanical response in a material that is effectively more ferroelectric-like. We note that recent theoretical studies have predicted similar effects in Cu-doped PMN-PT,<sup>[41]</sup> and such a combination of effects is advantageous for high-power and -temperature applications.

The question remains, however, as to why such large epitaxial strains cannot fully overcome or quench the relaxor order and why the strained systems exhibit stronger electromechanical responses. To address this question, we return to the MD simulations and extract the so-called time-delay-averaged-autocorrelation angle which probes the dynamic nature of dipoles by measuring the changes in alignment of each lead-ion dipole averaged over all waiting times (Experimental Section).

As such, small and large values of the autocorrelation angle refer to dipoles whose directions are relatively more stable (hence more ferroelectric-like) and unstable (hence more paraelectric-like) with time. This information, in turn, can help explain where the persistent disorder in our system arises. To better represent the differences in the dynamics of different local environments, we have broken down the total autocorrelation-angle distributions into contributions from lead ions in five chemically distinct local substructure cells (defined by different combinations of B-site cations surrounding one lead cation), including: 1)  $\text{PbMg}_{1/2}\text{Nb}_{1/2}\text{O}_3$  (magnesium-rich), 2)  $\text{PbMg}_{3/8}\text{Nb}_{1/2}\text{Ti}_{1/8}\text{O}_3$ , 3)  $\text{PbMg}_{1/4}\text{Nb}_{1/2}\text{Ti}_{1/4}\text{O}_3$ , 4)  $\text{PbMg}_{1/8}\text{Nb}_{1/2}\text{Ti}_{3/8}\text{O}_3$ , and 5)  $\text{PbNb}_{1/2}\text{Ti}_{1/2}\text{O}_3$  (titanium-rich) (Figure 5a). In turn, for each unit-cell chemistry, we can explore the strain evolution of their autocorrelation-angle distributions wherein we graph the distribution for that cell in the low-, intermediate-, and high-strain states (Figure 5b–f, corresponding to the unit cell directly above). The overall autocorrelation-angle distributions can be separated into two groups. The first behavior is that observed for the unit cells with only two different types of B-site cations (i.e., magnesium- and titanium-rich unit cells; Figure 5b,f) which show monotonic shifts of the autocorrelation-angle distributions to lower angles (i.e., become more ferroelectric-like) with increasing strain. This is especially surprising for the magnesium-rich cells which are strongly relaxor-like at zero strain. The second behavior is seen for all unit cells containing a mixture of magnesium, niobium, and titanium (Figure 5c–e) where the autocorrelation-angle distributions show a transition to two distinct peaks with increasing strain suggesting a fraction of cells with a smaller (i.e., more ferroelectric-like) or larger (i.e., more paraelectric-like) average deviation angle. In all cases, the high-strain state induces a shift of the two peaks to lower angles, indicating enhancement of ferroelectric behavior (Figure 5c–e). For example, focusing on the autocorrelation-angle distributions for the  $\text{PbMg}_{1/8}\text{Nb}_{1/2}\text{Ti}_{3/8}\text{O}_3$  unit cells (Figure 5e), it is observed that upon transitioning from the low-strain state, wherein there is a broad distribution with a single peak, to the intermediate-strain state results in a bifurcation of the peak into distributions centered at both larger and smaller angles. Upon increasing the strain further, those two peaks remain, but are shifted toward lower angles. This has important implications for understanding why the large applied compressive strains do not fully quench relaxor behavior and can even enhance material susceptibility. The data suggest that there are certain local chemical configurations of the same overall unit-cell chemistry that respond differently to the applied biaxial compression. Said another way, by locally varying the placement of the B-site cations relative to the strain, we can create some unit cells that become more ferroelectric (i.e., exhibit smaller angles) and some that become more paraelectric (larger angles). The larger angle peaks also indicate stronger scattering of lead displacements in the intermediate-strain state result in enhanced polarization (Figure 4a), as previously shown in PMN-PT doped with transition metals.<sup>[41]</sup> More broadly, this enhances the competition between relaxor and ferroelectric behavior which is directly related to the enhancement of electromechanical response (Figure 4b).<sup>[42]</sup> This is akin to prior work wherein the largest electromechanical responses

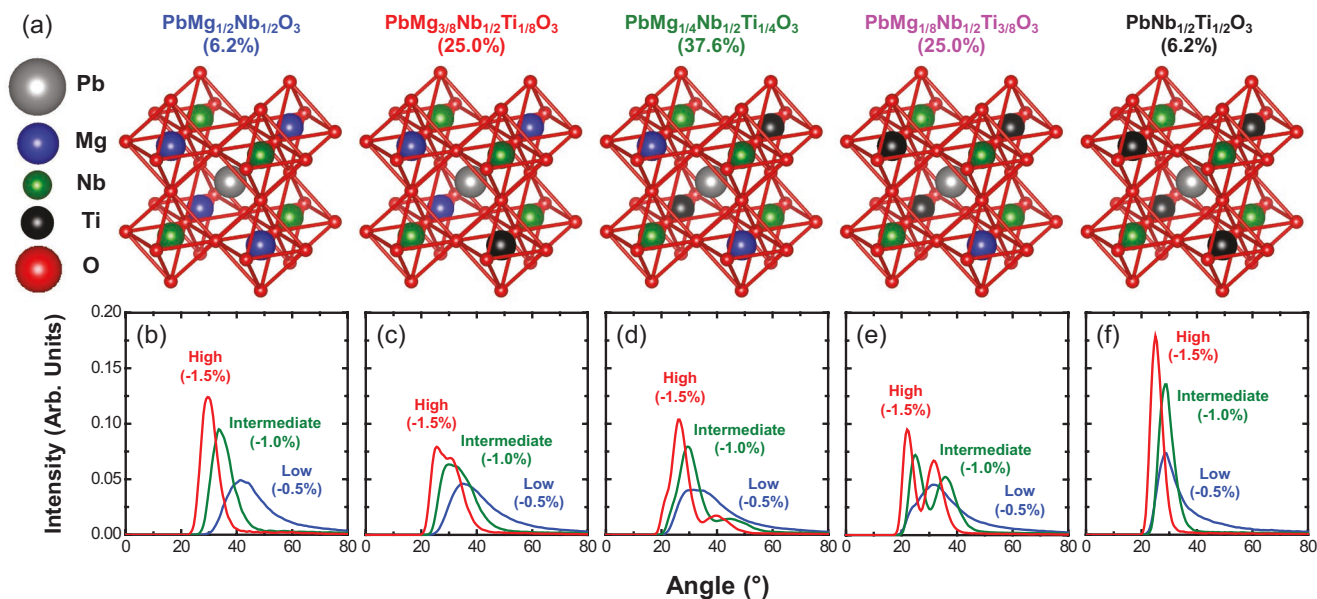


**Figure 5.** Strain evolution of autocorrelation-angle distributions for various local unit-cell chemistries and configurations. a) Schematic of the five substructure cells in PMN-PT. The percentages in parentheses are the relative populations of each substructure in the MD simulation. Each substructure is defined by the nearest *B*-site cation neighbors to one lead ion. b–f) Autocorrelation-angle distributions for lead ions in the five substructure cells of PMN-PT in (a). Each distribution is from the unit-cell type directly above.

were observed when the strength of relaxor behavior of PMN-PT is the weakest (i.e.,  $\Delta T_{\text{disp}} \approx 0$  °C) and the competition between relaxor and ferroelectric behavior is the strongest near the morphotropic phase boundary.<sup>[10]</sup> This understanding that different chemical configurations can have different tendency toward ferroelectric and/or paraelectric behavior could provide a guidance to the atomic-level design of new high-performance versions of even classic relaxor materials.

Ultimately, these studies provide new insights into the nature of relaxor behavior and the importance of the competition between relaxor and ferroelectric behavior in driving strong effects. Again, diffuse-scattering experiments reveal an evolution from butterfly- to disc-shaped patterns and an increase in the correlation length with increasing compressive strain that is subsequently connected to marked changes in the local-polar order. With increasing strain, the polar structure evolves from a complex, small-scale, multidomain structure to a larger, net up- and down-poled structure that still contains in-plane disorder. The changes in the local-polar order are accompanied by increases in  $T_b$ ,  $T_m$ , and the intermediate temperature  $T^*$  and a decrease of the frequency dispersion of  $T_m$  and corresponding increase in the coercive field—all suggestive of strain weaken the relaxor behavior. This does not, however, come at the expense of the electromechanical response which is also enhanced. Analysis of the dynamic evolution of dipole alignment in the simulations reveals that while, for most unit-cell chemistries and configurations, strain drives a tendency toward more ferroelectric-like order, there are certain unit cells which become more disordered under strain resulting in stronger competition between ordered and disordered regions and enhanced overall susceptibility to applied stimuli. Ultimately, this implies that deterministic creation of specific local chemical configurations could be an

effective way to enhanced relaxor performance even in classic materials and could provide a new approach to the design of materials.

## Experimental Section

**Epitaxial Thin-Film Growth:** Pulsed-laser deposition using a KrF excimer laser (248 nm, LPX 300, Coherent) was used to grow 55 nm  $0.68\text{Pb}(\text{Mg}_{1/3}\text{Nb}_{2/3})\text{O}_3\text{--}0.32\text{PbTiO}_3$  (PMN-PT)/25 nm  $\text{Ba}_{0.5}\text{Sr}_{0.5}\text{RuO}_3$  (BSRO) heterostructures on  $\text{NdScO}_3$ ,  $\text{SmScO}_3$ , and  $\text{GdScO}_3$  (110) substrates (CrysTec GmbH). The PMN-PT growth was carried out at a heater temperature of 600 °C in a dynamic oxygen pressure of 200 mTorr with a laser fluence of  $1.8 \text{ J cm}^{-2}$  and a laser repetition rate of 2 Hz from a ceramic target (Praxair) of the same composition with 10% lead excess to compensate for lead loss during growth. The BSRO growth was carried out at temperature of 750 °C in a dynamic oxygen pressure of 20 mTorr with a laser fluence of  $1.85 \text{ J cm}^{-2}$  and a laser repetition rate of 3 Hz from a ceramic target (Praxair) of the same composition. Following the growth, the samples were cooled to room temperature at  $5 \text{ °C min}^{-1}$  in a static oxygen pressure of 700 Torr.

**Structural Characterization:** X-ray  $\theta$ - $2\theta$  line scans and 2D reciprocal space mapping studies were conducted with a high-resolution X-ray diffractometer (X'pert Pro2, PANalytical). Synchrotron X-ray 3D reciprocal space mappings were conducted using a Huber 4-circle diffractometer and Pilatus 100K pixel detector with X-ray energy of 16 keV at beamline 33-BM-C at the Advanced Photon Source, Argonne National Laboratory. For the temperature-dependent diffuse-scattering measurements, the sample was mounted on a heating stage which goes up to 400 °C in air.

**Electrical Measurements:** Electrical measurements were performed on circular capacitor structures of PMN-PT films with symmetric BSRO top and bottom electrodes. For top electrode growth, substrate temperature was reduced to 550 °C to avoid the volatilization of lead, while the other growth parameters were the same as for the growth of the bottom electrode. The patterned circular top electrodes were 100 nm thick and 25  $\mu\text{m}$  in diameter and were deposited by means of a MgO

hard-mask technique.<sup>[43]</sup> The temperature-dependent dielectric constant measurements and capacitance-DC bias ( $C-V$ ) sweep were performed using an impedance analyzer (E4990A, Keysight Technologies). During  $C-V$  sweeps, the capacitance was measured by driving the top electrode with an AC voltage of 5 mV at a frequency of 10 kHz while the DC field is swept from  $\pm 200$  kV cm<sup>-1</sup> in both directions. The temperature-dependent dielectric constant was measured from room-temperature to 400 °C by driving the top electrode with an AC voltage of 5 mV from 1 to 100 kHz. A small DC bias, corresponding to the average of the field at which the capacitance is maximum during sweep-up and sweep-down in  $C-V$  measurements (Figure S7, Supporting Information) was applied to compensate for the imprint during the temperature-dependent dielectric constant measurement.<sup>[44]</sup> Room-temperature polarization-electric field hysteresis loops were measured at a frequency of 10 kHz using a Precision Multiferroic tester (Radiant Technologies). Room-temperature displacement-voltage bipolar hysteresis loops were measured at a frequency of 0.2 Hz via piezoresponse force microscopy using a MFP-3D (Asylum Research).

**Molecular-Dynamics Simulations:** Canonical-ensemble (NVT) MD simulations of the PMN-PT were conducted for a  $72 \times 72 \times 72$  perovskite-type supercell with 500 ps equilibrium run and 2 ns production time using a bond-valence-based interatomic potential.<sup>[45,46]</sup> The temperature was controlled by the Nosé-Hoover thermostat with a thermal inertia parameter  $M_s = 0.0207$  amu. The distribution of  $B$ -cations and potentials was the same as those used in ref. [8]. The lattice parameters for the 0.5%, 1.0%, and 1.5% strain states were  $a = b = 28.8576$  nm with  $c/a = 1.008$ ,  $a = b = 28.6992$  nm with  $c/a = 1.0248$ , and  $a = b = 28.5696$  nm with  $c/a = 1.0391$ , respectively. The instantaneous local polarization,  $\mathbf{P}_u(t)$ , for each unit cell is calculated as  $\mathbf{P}_u(t) = \frac{1}{V_u} \left( \frac{1}{8} \mathbf{Z}_A^* \sum_{i=1}^8 \mathbf{r}_{A,i}(t) + \mathbf{Z}_B^* \mathbf{r}_B(t) + \frac{1}{2} \mathbf{Z}_O^* \sum_{i=1}^6 \mathbf{r}_{O,i}(t) \right)$ ,

where  $V_u$  is the volume of a unit cell,  $\mathbf{Z}_A^*$ ,  $\mathbf{Z}_B^*$ , and  $\mathbf{Z}_O^*$  are the Born effective charges of  $A$ -site,  $B$ -site, and  $O$  atoms.<sup>[47]</sup>  $\mathbf{r}_{A,i}(t)$ ,  $\mathbf{r}_{B,i}(t)$ , and  $\mathbf{r}_{O,i}(t)$  are instantaneous atomic positions of  $A$ -site,  $B$ -site, and  $O$  atoms in a unit cell obtained from MD simulations. The computational diffuse-scattering patterns were calculated following the method employed in ref. [4]. It should be noted that pseudo-cubic symmetry was not applied in this work due to the tetragonal lattices induced by the strain. Instead, the average of the calculated diffuse-scattering about the 002- and 00 $\bar{2}$ -diffraction conditions was taken to remedy the roughly half lengths of  $c$ -axis in the MD simulations compared to the experimental thickness of 55 nm.

The time-delay-averaged angle correlation function in Figure 3 is calculated as

$$\frac{1}{2N_c} \frac{1}{\sqrt{\pi\sigma}} \sum_{i=1}^{N_c} \sum_{j=1}^2 \int e^{-\frac{(\theta-\theta_j(t'))^2}{\sigma}} dt' \quad (1)$$

where,  $N_c$  is the number of lead atoms in the PMN-PT,  $j$  denotes target atoms in  $n$ th neighbor cells along the  $\pm x$ ,  $\pm y$ , and/or  $\pm z$  direction from an origin lead atom,  $\theta$  is a given angle,  $\sigma$  is Gaussian width,  $t'$  is the time delay, and  $\theta_{ij}$  is the correlation function of angle formed by displacements between specific lead pairs above such that

$$\theta_{ij}(t') = \arccos \left( \int \hat{D}_i(t) \cdot \hat{D}_j(t+t') dt \right) \quad (2)$$

where  $\hat{D}(t)$  is the unit vector of a lead atom off-centering displacement as a function of time. The function is based on the equation in ref. [8], but the lead pairs were decomposed into the in-plane and out-of-plane directions for better representation in this work.

The autocorrelation of time-delay-averaged angles in Figure 5 is the same as in ref. [4]

$$\frac{1}{N_a} \frac{1}{\sqrt{\pi\sigma}} \sum_{i=1}^{N_a} \int e^{-\frac{(\theta-\theta_a(t'))^2}{\sigma}} dt' \quad (3)$$

where  $N_a$  is the number of lead atoms with values of 23296, 93151, 140255, 93349, and 23197 for the subgroups  $\text{Pb}(\text{Mg}_{1/2}\text{Nb}_{1/2})\text{O}_3$ ,  $\text{Pb}(\text{Mg}_{3/8}\text{Nb}_{1/2}\text{Ti}_{1/8})\text{O}_3$ ,  $\text{Pb}(\text{Mg}_{1/4}\text{Nb}_{1/2}\text{Ti}_{1/4})\text{O}_3$ ,  $\text{Pb}(\text{Mg}_{1/8}\text{Nb}_{1/2}\text{Ti}_{3/8})\text{O}_3$ , and  $\text{Pb}(\text{Nb}_{1/2}\text{Ti}_{1/2})\text{O}_3$ , respectively.

## Supporting Information

Supporting Information is available from the Wiley Online Library or from the author.

## Acknowledgements

J.K., H.T., and Y.Q. contributed equally to this work. This work was primarily funded by the U.S. Department of Energy, Office of Science, Office of Basic Energy Sciences, Materials Sciences and Engineering Division under Contract No. DE-AC02-05-CH11231 (Materials Project program KC23MP) for the development of the relaxor ferroelectric thin films. H.T. acknowledges support from the Office of Naval Research under grant N00014-17-1-2574. Y.Q. acknowledges support from the U.S. Department of Energy, Office of Basic Energy Sciences, under grant DE-FG02-07ER46431. A.R.D. acknowledges support from the U.S. Department of Energy, Office of Science, Office of Basic Energy Sciences, under Award Number DE-SC-0012375 for the growth of ferroelectric materials. A.F. acknowledges support from the Army Research Office under grant W911NF-14-1-0104. R.G. acknowledges support from the National Science Foundation under grant OISE-1545907. M.R.M. acknowledges support from the Gordon and Betty Moore Foundation's EPiQS Initiative, under grant GBMF5307. A.M.R. acknowledges support from the National Science Foundation under grant DMR-1719353. L.W.M. acknowledges support from the National Science Foundation under grant DMR-1708615. This research used resources of the Advanced Photon Source, a U.S. Department of Energy (DOE) Office of Science User Facility operated for the DOE Office of Science by Argonne National Laboratory under Contract No. DE-AC02-06CH11357. The authors acknowledge computational support from the NERSC of the U.S. Department of Energy and the HPCMO of the U.S. Department of Defense.

## Conflict of Interest

The authors declare no conflict of interest.

## Keywords

diffuse scattering, domain structure, polar nanodomains, relaxor ferroelectrics, strain control

Received: February 15, 2019

Revised: March 15, 2019

Published online:

- [1] L. E. Cross, *Ferroelectrics* **1994**, *151*, 305.
- [2] S. E. Park, T. R. Shrout, *J. Appl. Phys.* **1997**, *82*, 1804.
- [3] G. Burns, F. H. Dacol, *Phys. Rev. B* **1983**, *28*, 2527.
- [4] H. Takenaka, I. Grinberg, S. Liu, A. M. Rappe, *Nature* **2017**, *546*, 391.
- [5] H. Takenaka, I. Grinberg, A. M. Rappe, *Nat. Mater.* **2018**, *17*, 657.
- [6] B. Hehler, M. Al-Sabbagh, A. Al-Zein, J. Hlinka, *Phys. Rev. Lett.* **2016**, *117*, 155501.
- [7] A. Bosak, D. Chernyshov, S. Vakhruшев, M. Krisch, *Acta Crystallogr., Sect. A: Found. Crystallogr.* **2012**, *68*, 117.
- [8] H. Takenaka, I. Grinberg, A. M. Rappe, *Phys. Rev. Lett.* **2013**, *110*, 147602.
- [9] J. Hlinka, *J. Adv. Dielectr.* **2012**, *2*, 1241006.

- [10] M. J. Krogstad, P. M. Gehring, S. Rosenkranz, R. Osborn, F. Ye, Y. Liu, J. P. C. Ruff, W. Chen, J. M. Wozniak, H. Luo, O. Chmaissem, Z.-G. Ye, D. Phelan, *Nat. Mater.* **2018**, *17*, 718.
- [11] H. You, Q. M. Zhang, *Phys. Rev. Lett.* **1997**, *79*, 3950.
- [12] N. Takesue, Y. Fujii, M. Ichihara, H. Chen, *Phys. Rev. Lett.* **1999**, *82*, 3709.
- [13] G. Xu, Z. Zhong, H. Hiraka, G. Shirane, *Phys. Rev. B* **2004**, *70*, 174109.
- [14] G. Xu, G. Shirane, J. R. D. Copley, P. M. Gehring, *Phys. Rev. B* **2004**, *69*, 064112.
- [15] D. La-Orauttapong, J. Toulouse, Z.-G. Ye, W. Chen, R. Erwin, J. L. Robertson, *Phys. Rev. B* **2003**, *67*, 134110.
- [16] M. Matsuura, K. Hirota, P. M. Gehring, Z.-G. Ye, W. Chen, G. Shirane, *Phys. Rev. B* **2006**, *74*, 144107.
- [17] B. Chaabane, J. Kreisler, B. Dkhil, P. Bouvier, M. Mezouar, *Phys. Rev. Lett.* **2003**, *90*, 257601.
- [18] G. Xu, Z. Zhong, Y. Bing, Z.-G. Ye, G. Shirane, *Nat. Mater.* **2006**, *5*, 134.
- [19] G. Xu, J. Wen, C. Stock, P. M. Gehring, *Nat. Mater.* **2008**, *7*, 562.
- [20] Z. Kutnjak, J. Petzelt, R. Blinc, *Nature* **2006**, *441*, 956.
- [21] G. A. Samara, *Phys. Rev. Lett.* **1996**, *77*, 314.
- [22] P.-E. Janolin, B. Dkhil, M. Davis, D. Damjanovic, N. Setter, *Appl. Phys. Lett.* **2007**, *90*, 152907.
- [23] Q. Li, Y. Liu, V. Luzin, A. J. Studer, Y. Wan, Z. Li, L. Norén, R. L. Withers, Z. Xu, *J. Appl. Phys.* **2012**, *111*, 084110.
- [24] J. Wang, B. Eerd, T. Sluka, C. Sandu, M. Cantoni, X.-K. Wei, A. Kvasov, L. McGilly, P. Gemeiner, B. Dkhil, A. Tagantsev, J. Trodahl, N. Setter, *Nat. Mater.* **2015**, *14*, 985.
- [25] D. G. Schlom, L.-Q. Chen, C. B. Eom, K. M. Rabe, S. K. Streiffer, J.-M. Triscone, *Annu. Rev. Mater. Res.* **2007**, *37*, 589.
- [26] L. W. Martin, A. M. Rappe, *Nat. Rev. Mater.* **2017**, *2*, 16087.
- [27] A. R. Damodaran, J. C. Agar, S. Pandya, Z. Chen, L. Dedon, R. Xu, B. Apgar, S. Saremi, L. W. Martin, *J. Phys.: Condens. Matter* **2016**, *2*, 16087.
- [28] S. Prosandeev, D. Wang, L. Bellaiche, *Phys. Rev. Lett.* **2013**, *111*, 247602.
- [29] V. Nagarajan, C. S. Ganpule, B. Nagaraj, S. Aggarwal, S. P. Alpay, A. L. Roytburd, E. D. Williams, R. Ramesh, *Appl. Phys. Lett.* **1999**, *75*, 4183.
- [30] V. Nagarajan, S. P. Alpay, C. S. Ganpule, B. K. Nagaraj, S. Aggarwal, E. D. Williams, A. L. Roytburd, R. Ramesh, *Appl. Phys. Lett.* **2000**, *77*, 438.
- [31] P. Miao, Y. Zhao, N. Luo, D. Zhao, A. Chen, Z. Sun, M. Guo, M. Zhu, H. Zhang, Q. Li, *Sci. Rep.* **2016**, *6*, 19965.
- [32] M. Tyunina, J. Levoska, P.-E. Janolin, A. Dejneka, *Phys. Rev. B* **2013**, *87*, 224107.
- [33] J. C. Agar, R. V. K. Mangalam, A. R. Damodaran, G. Velarde, J. Karthik, M. B. Okatan, Z. H. Chen, S. Jesse, N. Balke, S. V. Kalinin, L. W. Martin, *Adv. Mater. Interfaces* **2014**, *1*, 1400098.
- [34] I. Grinberg, Y.-H. Shin, A. M. Rappe, *Phys. Rev. Lett.* **2009**, *103*, 197601.
- [35] I. Grinberg, P. Juhás, P. K. Davies, A. M. Rappe, *Phys. Rev. Lett.* **2007**, *99*, 267603.
- [36] S. D. Bu, M. K. Lee, C. B. Eom, *Appl. Phys. Lett.* **2001**, *79*, 3482.
- [37] S. K. Streiffer, J. A. Eastman, D. D. Fong, C. Thompson, A. Munkholm, M. V. Ramana Murty, O. Auciello, G. R. Bai, G. B. Stephenson, *Phys. Rev. Lett.* **2002**, *89*, 067601.
- [38] N. A. Pertsev, A. G. Zembilgotov, A. K. Tagantsev, *Phys. Rev. Lett.* **1998**, *80*, 1988.
- [39] F. Bai, N. Wang, J. Li, D. Viehland, P. M. Gehring, G. Xu, G. Shirane, *J. Appl. Phys.* **2004**, *96*, 1620.
- [40] B. Dkhil, P. Gemeiner, A. Al-Barakaty, L. Bellaiche, E. Dul'kin, E. Mojaev, M. Roth, *Phys. Rev. B* **2009**, *80*, 064103.
- [41] H. Tan, H. Takenaka, C. Xu, W. Duan, I. Grinberg, A. M. Rappe, *Phys. Rev. B* **2018**, *97*, 174101.
- [42] F. Li, D. Lin, Z. Chen, Z. Cheng, J. Wang, C. Li, Z. Xu, Q. Huang, X. Liao, L.-Q. Chen, T. R. ShROUT, S. Zhang, *Nat. Mater.* **2018**, *17*, 349.
- [43] J. Karthik, A. R. Damodaran, L. W. Martin, *Adv. Mater.* **2012**, *24*, 1610.
- [44] J. C. Frederick, T. H. Kim, W. Maeng, A. A. Brewer, J. P. Podkaminer, W. Saenrang, V. Vaithyanathan, F. Li, L.-Q. Chen, D. G. Schlom, S. Trolier-McKinstry, M. S. Rzchowski, C. B. Eom, *Appl. Phys. Lett.* **2016**, *108*, 132902.
- [45] S. Liu, I. Grinberg, H. Takenaka, A. M. Rappe, *Phys. Rev. B* **2013**, *88*, 104102.
- [46] I. Grinberg, V. R. Cooper, A. M. Rappe, *Nature* **2002**, *419*, 909.
- [47] M. Parrinello, A. Rahman, *Phys. Rev. Lett.* **1980**, *45*, 1196.